Progress In Electromagnetics Research M, Vol. 72, 135–143, 2018

Design of Wideband/Dual-Wideband/Tri-Band BPF Based on a Penta-Mode Resonator

Man Zhang[1], Yang Xiong[1], Li-Tian Wang[1], Sheng-Hui Zhao[1], Li Gong[1], Hui Li[1], Jian Xing[1], and Ming He[1, 2, *]

Abstract—In this paper, a stub-loaded penta-mode resonator (PMR) with its analysis, characterization and applications for bandpass filter (BPF) is presented. Even-/odd-mode analysis method is employed to analyze the PMR which exhibits five transmission poles (TPs) and three inherent transmission zeros (TZs). By changing the dimension parameters of the resonator, TPs and TZs can be flexibly controlled, and wideband/dual-wideband/tri-band BPF has been designed successfully utilizing the same configuration. For validation, all these three filters are fabricated and measured, and the measured results are in good agreement with the simulated ones.

1. INTRODUCTION

Recently, with the rapid development of high data-rate multiservice communication systems, single-/multi-band BPFs operating over wide frequency ranges are desperately demanded to enhance the performance of radio-frequency front end. Much efforts have been paid to investigate the BPFs possessing compact size, simple structure, planar configuration, good passband selectivity, and high suppression characteristics out of the passband. Up to now, a variety of topology structures and design methods have been studied. In [1–5], wideband BPFs are proposed, and dual-band BPFs are presented in [6–8], Moreover, in [9–13], tri-band BPFs are studied. Although these filters exhibit their merits, they also suffer from many drawbacks. For example, the BPFs in [2, 3, 9] are not planar implementation, i.e., defected ground structure is employed in [2], while multilayer structure is utilized in [3] and [9], which makes the fabrication procedure more complex. Two or more resonators are utilized in the multiband BPFs proposed in [6, 8, 12, 13], which leads to large circuit size. Besides, to the authors' knowledge, very few works about the resonating structure which can be utilized for both wideband and multiband BPFs are reported.

In this work, our main effort is made to provide a stub-loaded resonator which can simultaneously be utilized to design wideband/dual-wideband/tri-band BPF. These filters with its miniaturized circuit size, high out-of-band rejection and simple manufacture process are very attractive for the applications in modern communication systems. By even-/odd-mode method, the resonant characteristics of the PMR is analyzed due to its symmetric topological structure. Five TPs and three TZs are excited, which can be flexibly controlled by changing the impedance values and electrical lengths of the corresponding stubs. Five TPs can be arranged in one group with three TZs located beside them after fine tuning, then a wideband BPF is designed. Moreover, three TZs can divide five TPs into two different groups, and a dual-wideband BPF is obtained. Five TPs can also be divided into three groups by three TZs, thus a tri-band BPF is developed under the same configuration. For validation, all these three filters are fabricated on the substrate Rogers 4003c with $\varepsilon_r = 3.38$, $h = 0.508\,\text{mm}$, and $\tan\delta = 0.0027$, and

Received 7 May 2018, Accepted 13 August 2018, Scheduled 26 August 2018

* Corresponding author: Ming He (heming@nankai.edu.cn).

[1] College of Electronic Information and Optical Engineering, Nankai University, Tianjin 300350, China. [2] Tianjin Key Laboratory of Optoelectronic Sensor and Sensing Network Technology, Tianjin 300350, China.

they are measured by an Agilent E5071C network analyser. The good agreements between the full-wave EM simulations and the measurements verify the proposed design specification.

2. CHARACTERISTICS OF THE PROPOSED PMR

The ideal transmission line model (TLM) of the proposed PMR is presented in Fig. 1. The resonator is composed of a uniform impedance resonator with an open-ended cross-shaped stub attached to the middle and two identical open-ended stubs attached to the two symmetrical positions. The impedance and electrical lengths of the central cross-shaped stub are denoted by (Z_4, θ_4), (Z_5, θ_5) and (Z_6, θ_6), and the side stubs are indicated by (Z_2, θ_2). The classical even-/odd-mode analysis method is utilized to characterize the resonant properties of the PMR for its property of symmetry.

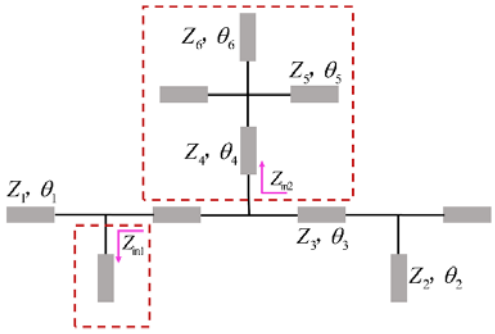

Figure 1. The ideal TLM of the PMR.

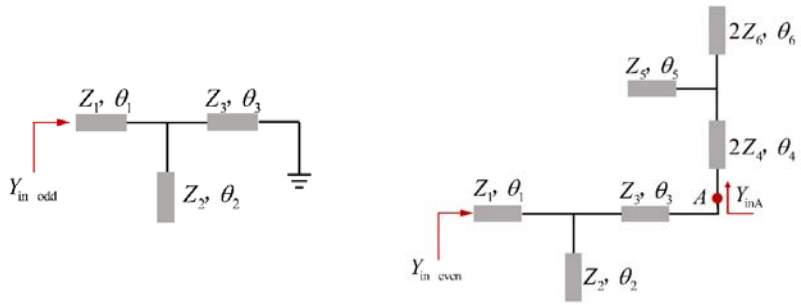

Figure 2. (a) Odd- and (b) even-mode equivalent circuits of the PMR.

When the odd resonant modes are excited, the central plane of the resonator can be equivalent to a perfect electric wall, thus the cross-shaped stub perturbation has no effect on them. For the even resonant modes, the central plane can be considered as a perfect magnetic wall. The odd-/even-mode equivalent circuits are shown as Fig. 2. And the input admittance of the odd-mode and even-mode can be expressed as:

$$Y_{\text{in-odd}} = Y_1 \frac{jY_2 \tan\theta_2 - jY_3 \cot\theta_3 + jY_1 \tan\theta_1}{Y_1 + \tan\theta_1 (Y_3 \cot\theta_3 - Y_2 \tan\theta_2)} \tag{1}$$

$$Y_{\text{in-even}} = \frac{Y_1 (Y_3 Y_{\text{inA}} + jY_3^2 \tan\theta_3) + j(Y_1 Y_2 \tan\theta_2 + Y_1^2 \tan\theta_1)(Y_3 + jY_{\text{inA}} \tan\theta_3)}{Y_1 (Y_3 + jY_{\text{inA}} \tan\theta_3) + jY_3 \tan\theta_1 (Y_{\text{inA}} + jY_3 \tan\theta_3) - Y_2 \tan\theta_1 \tan\theta_2 (Y_3 + jY_{\text{inA}} \tan\theta_3)} \tag{2}$$

where $Y_{\text{inA}} = Y_4 \dfrac{jY_4 \tan\theta_4 + 2jY_5 \tan\theta_5 + jY_6 \tan\theta_6}{2Y_4 - \tan\theta_4 (4Y_5 \tan\theta_5 + 2Y_6 \tan\theta_6)}$.

According to the resonance conditions, we can derive the following equations:

$$\mathrm{Im}\left(Y_{\text{in-odd}}\right) = 0 \tag{3}$$

$$\mathrm{Im}\left(Y_{\text{in-even}}\right) = 0 \tag{4}$$

As shown in Fig. 1, Z_{in1} and Z_{in2} denote the input impedance of the corresponding stubs enclosed by the red dotted rectangle respectively. If $Z_{in} = 0$ is satisfied at a certain frequency, the connection points are equivalent to virtual grounding. Thus, the transmission signal will be shorted out, and TZs are introduced to improve selection performance of the passband. TZs can be found by solving the following equations:

$$Z_{\text{in1}} = -jZ_2 \cot\theta_2 = 0 \tag{5}$$

$$Z_{\text{in2}} = -jZ_4 \frac{Z_5Z_6 - 2Z_4Z_6 \tan\theta_4 \tan\theta_5 - Z_4Z_5 \tan\theta_6 \tan\theta_4}{Z_5Z_6 \tan\theta_4 + 2Z_4Z_6 \tan\theta_5 + Z_4Z_5 \tan\theta_6} = 0 \tag{6}$$

The odd and even resonant modes as well as TZs can be solved referring to [14]. First of all, supposing a set of initial parameter values, θ_i, Z_i (i = 1, 2, 3, 4, 5, 6), f_0 (reference frequency for electrical length calculation) and frequency sweep range of interest. Then a corresponding resonator is determined, and frequencies excited by it are also fixed. The variation of θ_i or Z_i leads to the change of the resonator, and the new resonant frequencies within the frequency range can be found out through numerical calculation. Only the effect of a single parameter on the resonant frequencies is studied at once time, so all the other parameters are fixed as supposed values. The numerical calculation process for solving odd resonant modes is elaborated as an example, and the flow chart is shown as Fig. 3. When f_n within the frequency range is considered, all electrical lengths should be substituted by $\theta_i' = \theta_i f_n / f_0$ (i = 1, 2, 3, 4, 5, 6). If the updated θ_i' and Z_i make Eq. (3) satisfy, f_n is the first odd mode we are searching for. Traverse all frequencies within the frequency range, and we can obtain all the odd resonant modes. Replace Eq. (3) with Eq. (4), and we can find out the even resonant modes. If Eq. (3) is replaced by Eqs. (5) and (6), TZs can be obtained. As an example, the parameter values are supposed

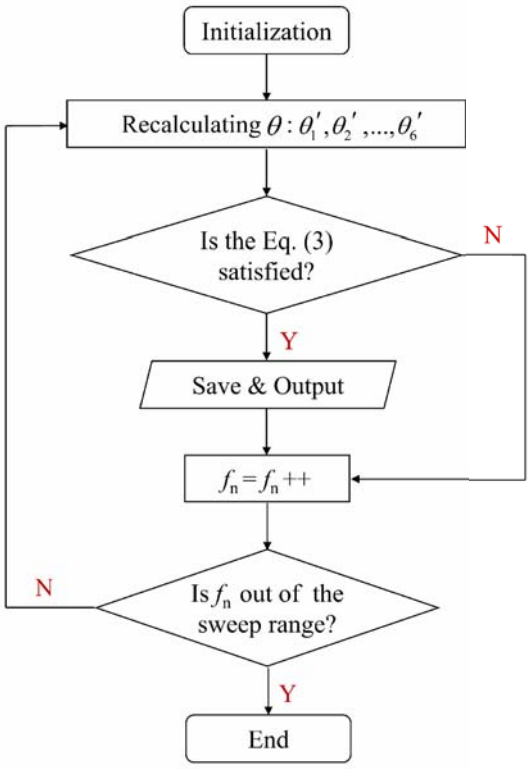

Figure 3. Flow chart of solving the odd resonant modes.

as: $Z_1 = 83.6\,\Omega$, $Z_2 = 92\,\Omega$, $Z_3 = 80\,\Omega$, $Z_4 = 35\,\Omega$, $Z_5 = 35\,\Omega$, $Z_6 = 130\,\Omega$, $\theta_1 = 65°$, $\theta_2 = 39°$, $\theta_3 = 18°$, $\theta_4 = 11°$, $\theta_5 = 50°$, $\theta_6 = 91.4°$, $f_0 = 3\,\text{GHz}$. Fig. 4 depicts the resonant properties versus varied θ_i, and Fig. 5 shows the influence on the resonant properties of varied Z_i ($i = 1, 2, 3, 4, 5, 6$).

As shown in Figs. 4(a) and (c), when θ_1 or θ_3 increases, f_{o1}, f_{o2}, f_{e2} and f_{e3} decrease. But f_{o2} and f_{e3} move closer to each other with θ_3 increasing. It is clear in Fig. 4(b) that f_{o2}, f_{e3} and f_{z3} decrease when θ_2 gets larger. It can be seen in Fig. 4(d) that f_{z2} decreases dramatically as θ_4 increases, whereas the other resonant modes are almost unchanged. This means that θ_4 can be employed to tune the position of f_{z2}. As indicated in Fig. 4(e) that θ_5 mainly affects f_{e2} and f_{z2}. And it is obviously observed from Fig. 4(f) that f_{e1} and f_{z1} move towards lower frequency with the increasing of θ_6.

According to Figs. 5(a) and (b), Z_1 and Z_2 mainly influence the value of f_{o2} and f_{e3}. As indicated in Fig. 5(c), f_{o2} and f_{e3} move towards each other with the increasing of Z_3. Fig. 5(d) illustrates that the variation of Z_4 mainly influences the location of f_{z1} and f_{z2}. It can be seen clearly in Fig. 5(e) that Z_5 can tune f_{e2} and f_{z2} without any influence on the others. As indicated in Fig. 5(f), Z_6 has no effect on the resonant frequencies when the value of Z_6 is relatively large. If Z_6 is less than $30\,\Omega$, f_{e2}, f_{z1} and f_{z2} change significantly with the variation of it.

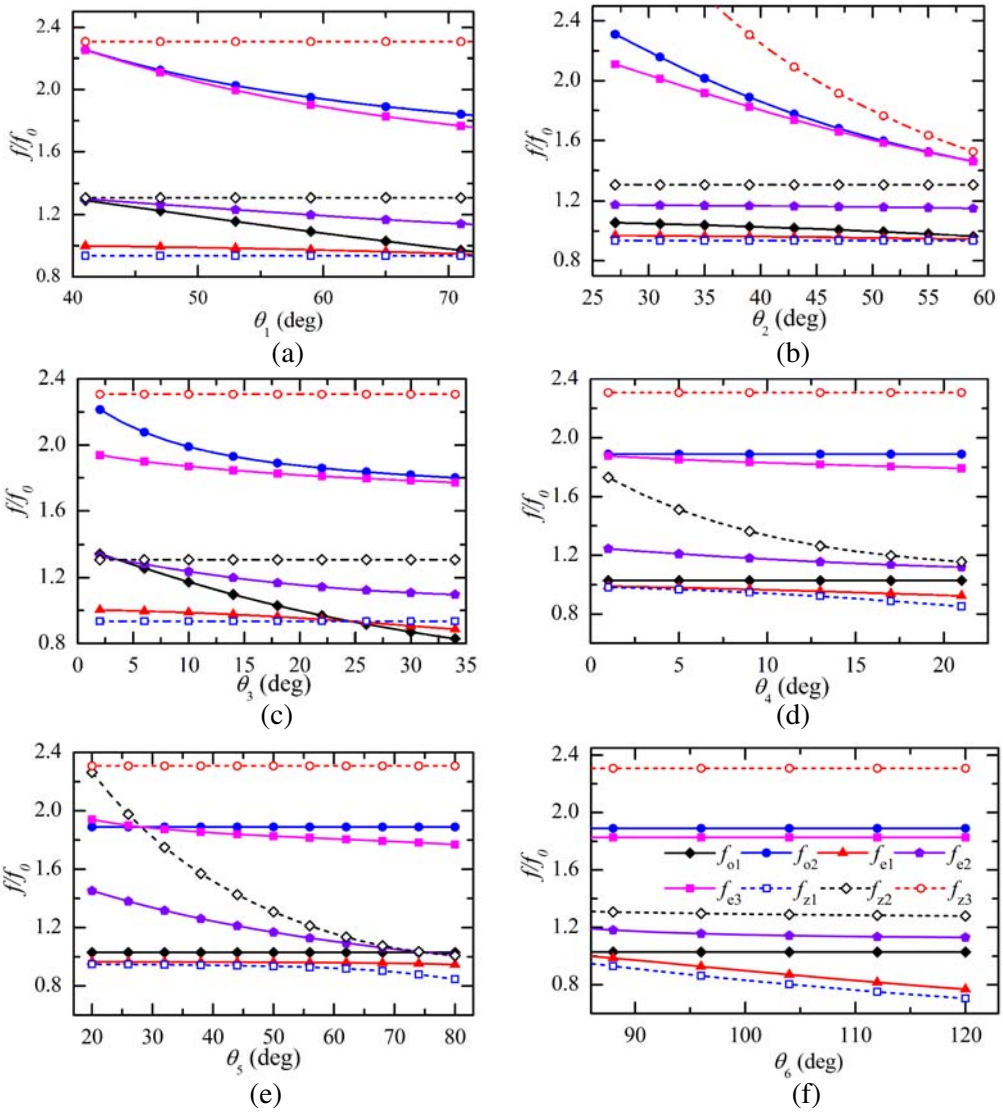

Figure 4. Variation of the resonant properties versus varied θ_i ($i = 1, 2, 3, 4, 5, 6$).

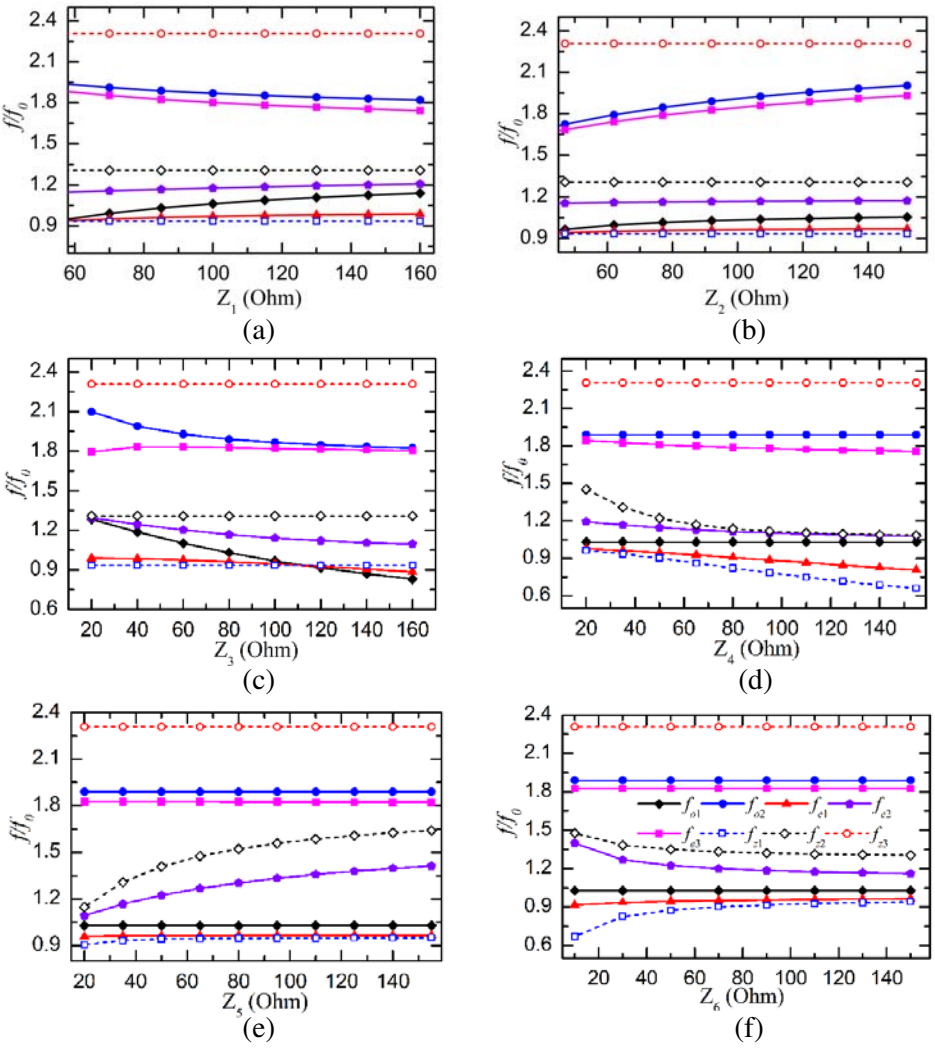

Figure 5. Variation resonance frequencies versus varied Z_i ($i = 1, 2, 3, 4, 5, 6$).

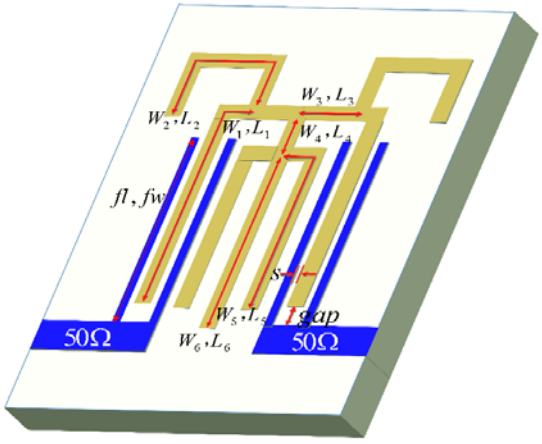

Figure 6. Topological layout of the proposed BPF.

3. FILTER DESIGN

Carefully arranging the resonant modes within the desired frequency range and introducing appropriate coupling strength between the resonator and the I/O ports by a pair of interdigital coupling lines, three BPFs can be developed under the same topological layout, which is depicted in Fig. 6.

3.1. Dual-Wideband BPF Design

According to the above analysis, the specific procedure of dual-wideband BPF design can be summed up as follows:

a) Change the impedance values and electrical lengths of the stubs to obtain the relationship: $f_{z1} < f_{e1} < f_{o1} < f_{e2} < f_{z2} < f_{e3} < f_{o2} < f_{z3}$. Then, f_{e1}, f_{o1} and f_{e2} form the first passband centered at f_{c1}, while f_{o2} and f_{e3} are applied to produce the second passband centered at f_{c2}.

b) Achieve desired f_{c2} by adjusting θ_1, θ_2, Z_1 and Z_2 according to Figs. 4(a)–(b) and Figs. 5(a)–(b).

c) Tune θ_3, θ_4, Z_3 and Z_4 to control the bandwidth of the second passband according to Figs. 4(c)–(d) and Figs. 5(c)–(d). Then, the second passband is obtained.

d) Adjustf_{c1} by changing θ_5, θ_6 and Z_6. And the bandwidth of the first passband can be controlled flexibly by changing the value of Z_5.

e) Introduce appropriate coupling strength by a pair of dual-finger feedlines.

Referring to the design procedure above, a dual-wideband BPF which can be utilized for WiMAX/WLAN applications is designed, simulated and manufactured. The optimized dimension parameters in Fig. 6 are shown as follows: $L_1 = 10.35$, $L_2 = 6.9$, $L_3 = 3.1$, $L_4 = 1.3$, $L_5 = 11.75$, $L_6 = 12.3$, $W_1 = 0.1$, $W_2 = 0.2$, $W_3 = 0.65$, $W_4 = 1.7$, $W_5 = 0.8$, $W_6 = 0.8$, $fw = 0.2$, $fl = 9.3$, $s = 0.25$, $gap = 0.6$ (The unit is millimeter). The overall circuit size is 14.2 mm × 16.35 mm (excluding the feedlines), i.e., approximately $0.29\lambda_g \times 0.33\lambda_g$, where λ_g is the guided wavelength at 3.75 GHz. As deduced in Fig. 7(a), the measured results agree well with the simulated ones. A photograph of the fabricated filter is represented in Fig. 7(b). The measured passbands of the filter which are centered at 3.75/5.86 GHz, have the minimum insertion losses (ILs) of 1.71 dB and 1.92 dB respectively, and the −3 dB fractional bandwidths (FBWs) of 11.2% and 18.9% are obtained. Within the passbands, return losses (RLs) are better than 11.2 dB. Three TZs can be clearly observed in Fig. 7(a), which are located at 3.34 GHz, 4.0 GHz and 7.2 GHz. Over 15 dB, the out-of-band rejection level from 7 GHz to 14 GHz is realized. The dual-wideband BPF possesses wide stopband suppression, small size, good passband selectivity and simple manufacture process.

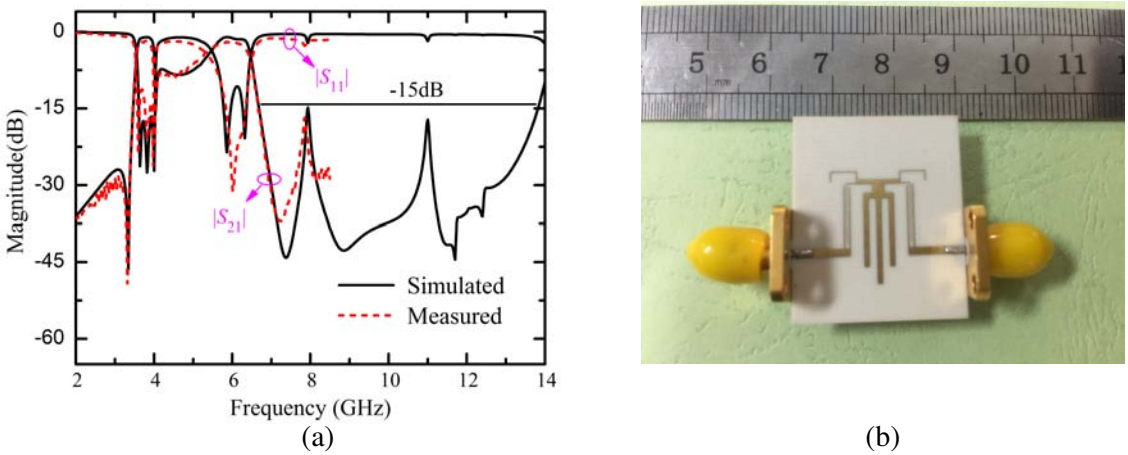

Figure 7. (a) Measured and simulated frequency response of the filter. (b) Photograph of the fabricated filter.

3.2. Wideband BPF Design

As discussed in Fig. 4(e), f_{e3} and f_{z2} increase with the decrease of θ_5, whereas f_{o2} keeps constant. When θ_5 is less than 30° the relationship of $f_{z1} < f_{e1} < f_{o1} < f_{e2} < f_{o2} < f_{e3} < f_{z2} < f_{z3}$ can be achieved. Referring to the design procedure of dual-wideband BPF, a wideband BPF can be designed. Correspondingly, the dimension parameters in Fig. 6 are given as follows: $L_1 = 8.9$, $L_2 = 6.2$, $L_3 = 2.4$, $L_4 = 3$, $L_5 = 1$, $L_6 = 14.8$, $W_1 = 0.1$, $W_2 = 0.1$, $W_3 = 0.3$, $W_4 = 0.1$, $W_5 = 0.1$, $W_6 = 0.1$, $fw = 0.1$, $fl = 9$, $s = 0.1$, $gap = 0.9$ (Unit: mm). The overall circuit size is 11 mm × 6 mm (excluding the feedlines), i.e., approximately $0.16\lambda_g \times 0.31\lambda_g$, where λ_g is the guided wavelength at 5.2 GHz.

Figure 8 depicts the S-parameter curves of the wideband BPF, and we can figure out that the first-, third-, fourth-, fifth-, and seventh-order poles are brought out by the PMR. Meanwhile, the second and sixth poles are contributed by the two $\lambda_g/4$ coupled line sections with enhanced coupling degree. Fig. 9 shows a photograph of the fabricated filter and its results. The measured results are in good agreement with the simulated ones. The −3 dB FBW of the wideband BPF is about 87%. The measured minimum IL is 1.3 dB, and the RL is better than 15 dB. It is worth mentioning that two inherent TZs close to the passband greatly improve the selection performance of the filter. The wideband BPF exhibits compact circuit size and high out-of-band rejection skirts.

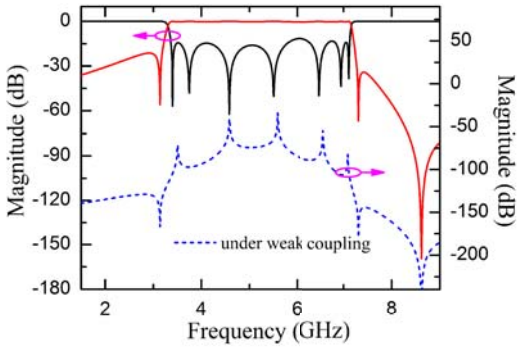

Figure 8. S-parameter curves of the wideband BPF with approperiate coupling strength and with weak coupling strength.

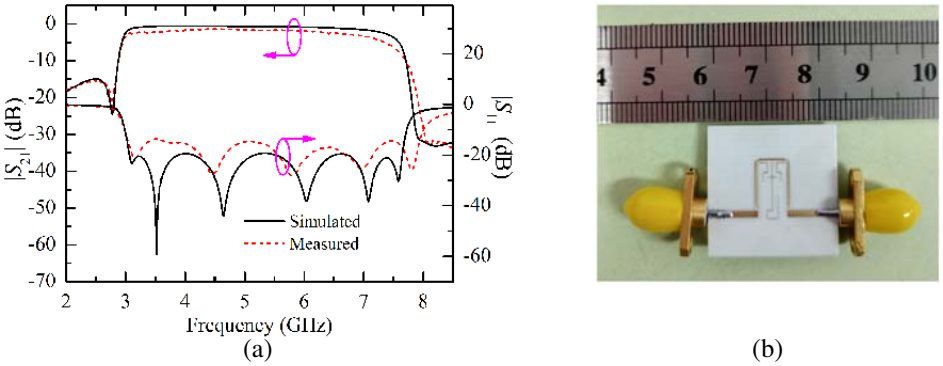

Figure 9. (a) Measured and simulated frequency response of the wideband BPF. (b) Photograph of the fabricated wideband BPF.

3.3. Triband BPF Design

If θ_3 is larger than 26° as Fig. 4(c) shows, five resonate modes can be divided into three different groups ($f_{o1} < f_{e1} < f_{z1} < f_{e2} < f_{z2} < f_{e3} < f_{o2} < f_{z3}$). Thus a tri-band BPF can be developed by appropriate design procedure which is similar to dual-wideband BPF design. The corresponding parameters in

Fig. 6 are given as follows: $L_1 = 14.3$, $L_2 = 5.2$, $L_3 = 5.2$, $L_4 = 1.65$, $L_5 = 5.4$, $L_6 = 14.85$, $W_1 = 0.4$, $W_2 = 0.2$, $W_3 = 0.5$, $W_4 = 0.6$, $W_5 = 1.5$, $W_6 = 0.6$, $fw = 0.1$, $fl = 11.5$, $s = 0.25$, $gap = 0.95$ (Unit: mm). The overall circuit size is 16.4 mm × 20.8 mm (excluding the feedlines), i.e., approximately $0.21\lambda_g \times 0.26\lambda_g$, where λ_g is the guided wavelength at 2.3 GHz. The comparison of the electromagnetic simulation results and the measured results is deduced in Fig. 10(a). Fig. 10(b) is a photograph of the tri-band BPF. Some discrepancies between the simulated and measured results may be attributed to fabrication tolerance and introduction of the SMA connector. The measured minimum ILs are 1.7, 2.6 and 4 dB, while the RLs are better than 16 dB. The filter exhibits good out-of-band suppression performance. The tri-band filter centered at 2.3/3.8/5.8 GHz can be applied in WiFi/WiMAX/WLAN communication systems.

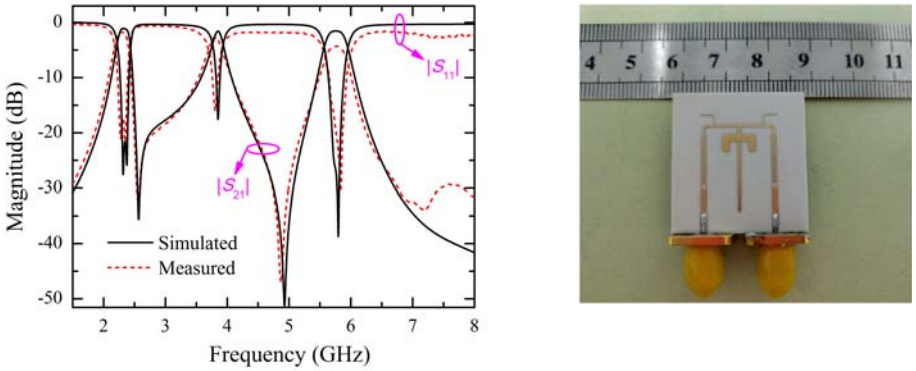

Figure 10. (a) Measured and simulated frequency response of the tri-band BPF. (b) Photograph of the fabricated tri-band BPF.

In addition, a performance comparison of this work and some previously published works is provided in Table 1. It can be observed that the proposed PMR can be utilized for different BPF designs based on a single resonator, which is rarely presented in earlier works.

Table 1. Performance comparison with referenced work.

Reference	Reported response for proposed resonating structure		No. of resonator	Planar structure
	Wide frequency response	Multiband response		
[2]	√	×	2	×
[4]	√	×	4	×
[8]	×	√	2/3	√
[9]	×	√	3	×
This work	√	√	1	√

4. CONCLUSION

In this paper, a PMR containing three flexibly controllable TZs is proposed. Even-/odd-mode analysis method is employed to analyze the PMR for its symmetric characteristics. The TZs and TPs can be arranged by adjusting the impedance values and the electrical lengths properly. Therefore, the PMR can be utilized to form wideband/dual-wideband/tri-band BPF under the same configuration. Three BPFs are fabricated, and the measurement results are almost identical to the simulation results, which validates the proposed design method. Flexibly controlled resonating modes and high passband selectivity bring the proposed PMR an alluring prospect in multiservice wireless communication systems.

REFERENCES

1. Huang, F., J. P. Wang, J. L. Li, and W. Wu, "Compact microstrip wideband bandpass filter with high selectivity," *Electronics Letterers*, Vol. 52, No. 8, 626–628, 2016.
2. Peng, B., S. F. Li, J. F. Zhu, Q. Y. Zhang, L. Deng, Q. S. Zeng, and Y. Gao, "Wideband bandpass filter with high selectivity based on dual-mode DGS resonator," *Microwave and Optical Technology Letters*, Vol. 58, No. 10, 2300–2303, 2016.
3. Périgaud, A., S. Bila, S. Verdeyme, D. Baillargeat, and D. Kaminsky, "Multilayer interdigital structures for compact bandpass filters providing high selectivity and wideband rejections," *IEEE Microwave and Wireless Components Letters*, Vol. 24, No. 2, 93–95, 2014.
4. Yang, L., W. W. Choi, K. W. Tam, and L. Zhu, "Novel wideband bandpass filter with dual notched bands using stub-loaded resonators," *IEEE Microwave and Wireless Components Letters*, Vol. 27, No. 1, 25–27, 2017.
5. Yechou, L., A. Tribak, M. Kacim, J. Zbitou, and A. M. Sanchez, "A novel wideband bandpass filter using coupled lines and T-shaped transmission lines with wide stopband on low-cost substrate," *Progress In Electromagnetics Research C*, Vol. 67, 143–152, 2016.
6. Tian, Q., C. Wang, and N. Y. Kim, "A compact dual-wideband bandpass filter using two triple-mode resonators for S-band applications," *Microwave and Optical Technology Letters*, Vol. 57, No. 1, 153–157, 2015.
7. Liu, H. W., S. Li, X. H. Guan, B. P. Ren, J. H. Lei, and Y. Wang, "Compact dual-wideband bandpass filter with multimode resonator," *ETRI Journal*, Vol. 36, 163–166, 2014.
8. Wang, Z. J., C. Wang, and N. Y. Kim, "Dual-/triple-wideband microstrip bandpass filter using independent triple-mode stub-loaded resonator," *Microwave and Optical Technology Letters*, Vol. 60, No. 1, 56–64, 2018.
9. Majidfar, S. and M. Hayati, "New approach to design a compact triband bandpass filter using a multilayer structure," *Turkish Journal of Electrical Engineering & Computer Sciences*, Vol. 25, 4006–4012, 2017.
10. Lu, D., N. S. Barker, and X. H. Tang, "Compact and independently-design tri-band bandpass filter with bandwidth and return loss control," *Electronics Letterers*, Vol. 52, No. 24, 1992–1994, 2016.
11. Xu, J., "Compact microstrip tri-band bandpass filter using new stubs loaded stepped-impedance resonator," *IEEE Microwave and Wireless Components Letters*, Vol. 26, No. 4, 249–251, 2016.
12. Liu, H. W., F. Liu, B. P, Ren, A. P. Yao, X. Xiao, Y. X. Yang, and X. H. Guan, "Compact tri-band bandpass filter using asymmetric stub-loaded stepped-impedance resonator with multiple transmission zeros," *International Journal of Microwave and Wireless Technologies*, Vol. 9, No. 7, 1453–1457, 2017.
13. Li, W. P., Z. X. Tang, H. D. Lin, and X. Cao, "A novel planar tri-band bandpass filter using stub-loaded resonators," *IEICE Electronics Express*, Vol. 13, No. 18, 1–8, 2016.
14. Xiong, Y., L. T. Wang, W. Zhang, F. Zhang, D. D. Pang, M. He, X. J. Zhao, and L. Ji, "Design of dual-band bandpass filter with closely spaced passbands and multiple transmission zeros," *Progress In Electromagnetics Research Letters*, Vol. 70, 45–51, 2017.